# Title: A Tetrahedral Neptunium(V) Complex

**Authors:** Julie E. Niklas,[1+] Kaitlyn S. Otte,[1+] Chad M. Studvick,[2] Sabyasachi Roy Chowdhury,[3] Bess Vlaisavljevich,[3] John Bacsa,[1] Ivan A. Popov,[2]* and Henry S. La Pierre[1,4,5]*

**Affiliations:**

[1]School of Chemistry and Biochemistry, Georgia Institute of Technology, Atlanta, Georgia 30332-0400, United States.

[2]Department of Chemistry, The University of Akron, Akron, Ohio 44325-3601, United States.

[3]Department of Chemistry, University of South Dakota, Vermillion, South Dakota, 57069, United States.

[4]Nuclear and Radiological Engineering and Medical Physics Program, School of Mechanical Engineering, Georgia Institute of Technology, Atlanta, Georgia 30332-0400, United States.

[5]Physical Sciences Division, Pacific Northwest National Laboratory, Richland, WA 99352, United States.

[+]K.S.O. and J.E.N. contributed equally; the first authors agreed to allow order change for listing on CVs as per group policy.

**Abstract: Neptunium is an actinide element sourced from anthropogenic production, and unlike naturally abundant uranium, its coordination chemistry is not well-developed in all accessible oxidation states. High-valent neptunium generally requires stabilization from at least one metal-ligand multiple bond, and departing from this structural motif poses a considerable challenge. We report a tetrahedral molecular neptunium(V) complex ($[Np^{5+}(NPC)_4][B(ArF_5)_4]$, 1-Np), (NPC = $[NP^tBu(pyrr)_2]^-$; $^t$Bu = $C(CH_3)_3$; pyrr = pyrrolidinyl ($N(C_2H_4)_2$); $B(ArF_5)_4$ = tetrakis(2,3,4,5,6-pentafluourophenyl)borate). Single-crystal X-ray diffraction, solution-state spectroscopic, and density functional theory studies of 1-Np and the product of its proton-coupled electron transfer (PCET) reaction, 2-Np, demonstrate the unique bonding that stabilizes this reactive ion and establishes the thermochemical and kinetic parameters of PCET in a condensed phase transuranic complex. The isolation of this four-coordinate, neptunium(V) complex reveals a fundamental reaction pathway in transuranic chemistry.**

## Main Text:

Across the mid-actinides (U-Pu), chemical oxidation becomes markedly more difficult with increasing atomic number, and the stabilization of higher-valent species of Np and Pu remains a significant challenge. Outside of ubiquitous actinyl (dioxo) or rare Np and Pu tetra(oxo) complexes, which can support the 5+, 6+, and 7+ oxidation states, high-valent, non-actinyl transuranic complexes are limited to a Np$^{5+}$ mono(oxo) complex[1] and a Np$^{5+}$ bis(imido) complex[2]. The latter complex features linear actinyl-like bonding of the *trans*-bis(imido) ligands[2]. In both cases, metal-ligand multiple bonding (MLMB) interactions are essential to stabilize the Np$^{5+}$ center. Reported molecular transuranic complexes with oxidation states higher than 4+ are exclusively supported by MLMB interactions or by high coordination numbers of electron-withdrawing ($F^-$) ligands[1-4], though extended solids and polymeric species have been identified[5-8]. We have previously developed imidophosphorane ligands to access and stabilize tetravalent lanthanide complexes[9-12], and have recently reported a homologous family of tetravalent Ce, U, and Np complexes[13,14]. These complexes present significantly cathodically shifted redox couples, which afford access to an isolable tetrahedral $U^{5+}$ species and to the first reported $Np^{5+/4+}$ non-aqueous redox couple[13]. The accessibility of this couple (-0.70 V *vs*. $Fc^{+/0}$) facilitates the development of synthetic methodology to isolate a tetrahedral, non-actinyl $Np^{5+}$ complex. Herein we report the synthesis and isolation of $[Np^{5+}(NPC)_4][B(ArF_5)_4]$, (NPC = $[NP^tBu(pyrr)_2]^-$; $^tBu$ = $C(CH_3)_3$; pyrr = pyrrolidinyl ($N(C_2H_4)_2$); $B(ArF_5)_4$ = tetrakis(2,3,4,5,6-pentafluourophenyl)borate), **1-Np** (Fig. 1, 2A). This complex is stable in the solid-state and undergoes a relatively slow, first-order proton-coupled electron transfer (PCET) reaction in THF to afford $[Np^{4+}(NPC)_3(HNPC)][B(ArF_5)_4]$, **2-Np** (Fig. 1, 2B).

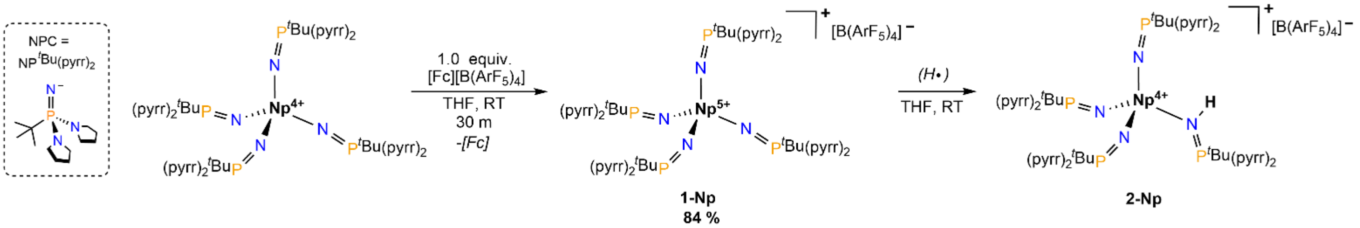

**Figure 1 | Synthesis of 1-Np and 2-Np.** Inert atmosphere synthesis of **1-Np** by outer-sphere one-electron oxidation of the $Np^{4+}$ species, and formation of **2-Np** by H· abstraction from solvent.

## Synthesis & characterization of 1-Np

Chemical oxidation of the tetravalent neptunium complex, $[Np^{4+}(NPC)_4]$, with $[Fc][B(ArF_5)_4]$ (Fc = ferrocene, $Cp_2Fe$), a fairly mild oxidant[15], results in the rapid color change of the solution from bright pink to deep golden-brown. The reaction time is limited to 30 minutes to mitigate loss of the product to subsequent reactivity with THF (*vide infra*). Following completion of the reaction, volatiles are removed, and the product residue is washed with pentane to remove ferrocene and then extracted into diethyl ether. Concentration of the solution and storage overnight at -35 °C gives **1-Np** as large brown-black crystals in 84% yield. The complex's identity and the $Np^{5+}$ oxidation state are confirmed by single crystal X-ray diffraction (SC-XRD) and electronic absorption and nuclear magnetic resonance (NMR) spectroscopy and are further supported by theoretical calculations.

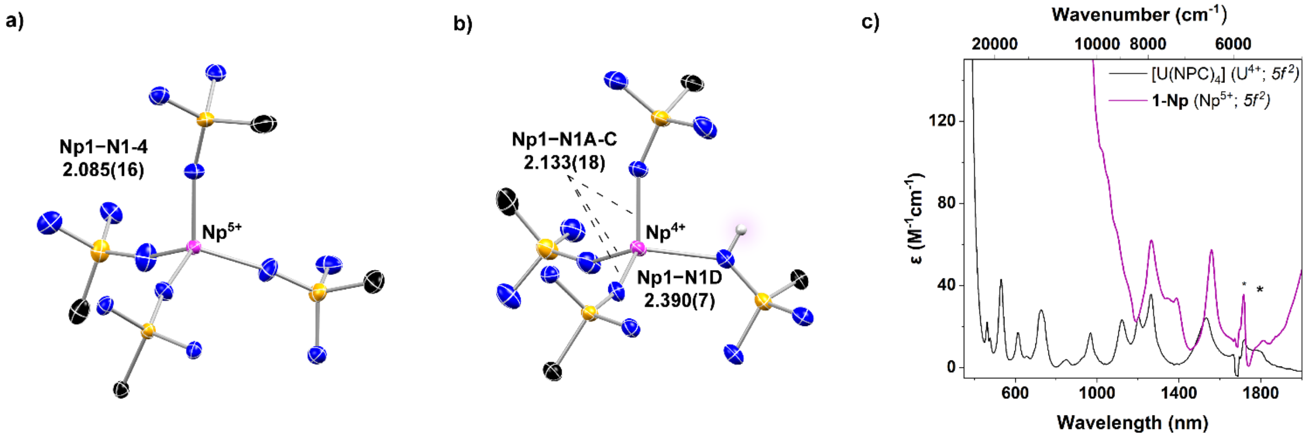

**Figure 2 | Structures and spectroscopy of compounds. a & b,** Molecular structures of **1-Np** (left) and **2-Np** (right) as determined by SC-XRD. Thermal ellipsoids are shown at 50% (atom colors: Np, pink; N, blue; P, orange; C, black; H, white). $[B(ArF_5)_4]$ anions, H atoms (except protonated ligand in **2-Np**) and all except quaternary C atoms of the cation omitted for clarity. **c)** Electronic absorption spectrum of $[Np^{5+}(NPC)_4][B(ArF_5)_4]$ **(1-Np)** (8.0 mM in THF) collected ~45 min after sample preparation, and $[U^{4+}(NPC)_4]$[13]. Cuvette was masked to 2mm. * denotes some contribution from light scattering and solvent overtone at 1718 nm.

**1-Np** crystallizes in the $P2_1/n$ space group and is isotypic with the structure of [$U^{5+}$(NPC)$_4$][B(ArF$_5$)$_4$] (**1-U**) [13]. The asymmetric unit contains one [$Np^{5+}$(NPC)$_4$]$^+$ cation and [B(ArF$_5$)$_4$]$^-$ anion (Fig. 2A, S16). The [$Np^{5+}$(NPC)$_4$]$^+$ cation is tetrahedral with a $\tau_4$ of 0.96 and an average N–Np–N angle of 109(2)°. The bond metrics compare well with those of **1-U**, which is also an unusual homoleptic, tetrahedral $An^{5+}$ complex (Extended Data Table 1). The Np−N distances of 2.085(16) Å are approximately 0.015 Å shorter than the average $U^{5+}$−N distance in line with the change in the effective ionic radii[16]. We have previously shown that the degree of pyramidalization among the two crystallographically unique pyrrolidinyl N atoms, in conjunction with the P–$N_{pyrr}$ length, is a useful reporter of oxidation state in these species[13,14]. This metric is described by the sum of angles around the pyrrolidinyl N atom, ΣN°, where more planar N atoms (ΣN° closer to 360°) are correlated with shorter P–N bond lengths and higher-oxidation state actinide centers. In **1-Np**, the average P–$N_{pyrr}$ distance of 1.667(11) Å encompasses two distinct groupings of values for the rigorously planar pyrrolidinyl N atoms (ΣN° = 359.6(2); P–$N_{planar}$ = 1.652(11) Å) and more pyramidalized N atoms (ΣN° = 345(2); P–$N_{pyram}$ = 1.669(8) Å). The same distribution is observed for **1-U**, and the pentavalent species are distinct from their tetravalent counterparts[13,14], which feature an evenly-dispersed range of ΣN° values between 343° and 360° (Fig. S21).

The electronic absorption spectrum of **1-Np** in THF (Fig. 2C) shows an intense charge transfer feature ($\lambda_{max}$ = 230 nm; $\varepsilon$ = 27,000 $M^{-1}cm^{-1}$) with a broad tail extending past 1000 nm (Fig. S1) and several weak *f-f* features in the NIR at 1260 nm ($\varepsilon$ = 60 $M^{-1}cm^{-1}$), 1560 ($\varepsilon$ = 60 $M^{-1}cm^{-1}$), and 1350-1390 nm (broad, unresolved; $\varepsilon$ = 30 $M^{-1}cm^{-1}$). The features at 1260 nm and 1560 nm are shared with those of the isovalent ($5f^2$) $U^{4+}$ complex, [$U^{4+}$(NPC)$_4$] [14], and are diagnostic of the $5f^2$ electron configuration for **1-Np**. The features at 1350-1390 nm indicate the formation of $Np^{4+}$ due to the PCET reaction with THF in the cuvette (See solution characterization)[17].

## 1-Np electronic structure & bonding

The calculated bond metrics for **1-Np** show good agreement with the experimental data, deviating by 0.0% and 0.8% for the Np–$N_{im}$ and P=$N_{im}$ bonds (Extended Data Table 1, Table S2). Analysis of molecular orbitals (MOs) provides more insight into the metal-ligand (M–L) bonding interactions in **1-Np** and is further employed for comparison with **1-U** to elucidate differences in their electronic structures (Fig. 3). The highest set of occupied MOs in both complexes describe a combination of M–$N_{im}$–P π bonding interactions and predominantly 2*p* lone pairs (LPs) on $N_{pyrr}$ atoms giving rise to subtle P–$N_{pyrr}$ π interactions. Orbitals describing the M–$N_{im}$ σ interactions are found approximately 2.5 eV lower in energy in both **1-Np** and **1-U** (Fig. S22, Table S3), with almost equal metal contribution (avg. 10.1% in **1-Np** and 10.2% in **1-U**), and comparable orbital characters (Table S3). The highest occupied MO (HOMO) of **1-Np** displays a ligand-dominant orbital (5.0% Np [2.8% 5*f*/1.1% 6*d*]), unlike **1-U**, which displays a metal-dominant orbital (84.3% U [78.6% 5*f*/5.6% 6*d*]), clearly describing the unpaired 5*f* electron on U (Fig. 3, Table S4). The two unpaired electrons anticipated for the $5f^2$ configuration of pentavalent **1-Np** are buried lower in energy and spread throughout the frontier ligand-dominant orbitals with increased 5*f* character (2.6%-29.8% in **1-Np** *vs*. 0.5%-10.0% in **1-U**; see representative orbitals in Fig. 3). The greater mixing of the metal-dominant orbitals with the closest in energy ligand-dominant orbitals is also noted for the tetravalent [$Np^{4+}$(NPC)$_4$] in comparison to [$U^{4+}$(NPC)$_4$] (Table S5). It occurs due to the substantial decrease in energy of the highest occupied 5*f* metal-dominant MOs. Specifically, HOMO of [$Np^{4+}$(NPC)$_4$] is 1.21 eV lower than that of [$U^{4+}$(NPC)$_4$], therefore the energy gap between the metal-dominant and ligand-dominant MOs decreases from 1.29 eV to 0.23 eV (Fig. S23, S24). This result suggests a greater availability of 5*f* electrons for oxidation of [$U^{4+}$(NPC)$_4$] compared to [$Np^{4+}$(NPC)$_4$], in line with the Mulliken spin density on the metal centers (Table S7). While this analysis indicates primarily metal-based oxidations of both $M^{4+}$ species, there is a smaller decrease in the spin density for the Np complexes*, i.e.*, 3.22 in [$Np^{4+}$(NPC)$_4$] to 2.42 in **1-Np** *vs.* 2.17 in [$U^{4+}$(NPC)$_4$] to 1.17 in **1-U**.

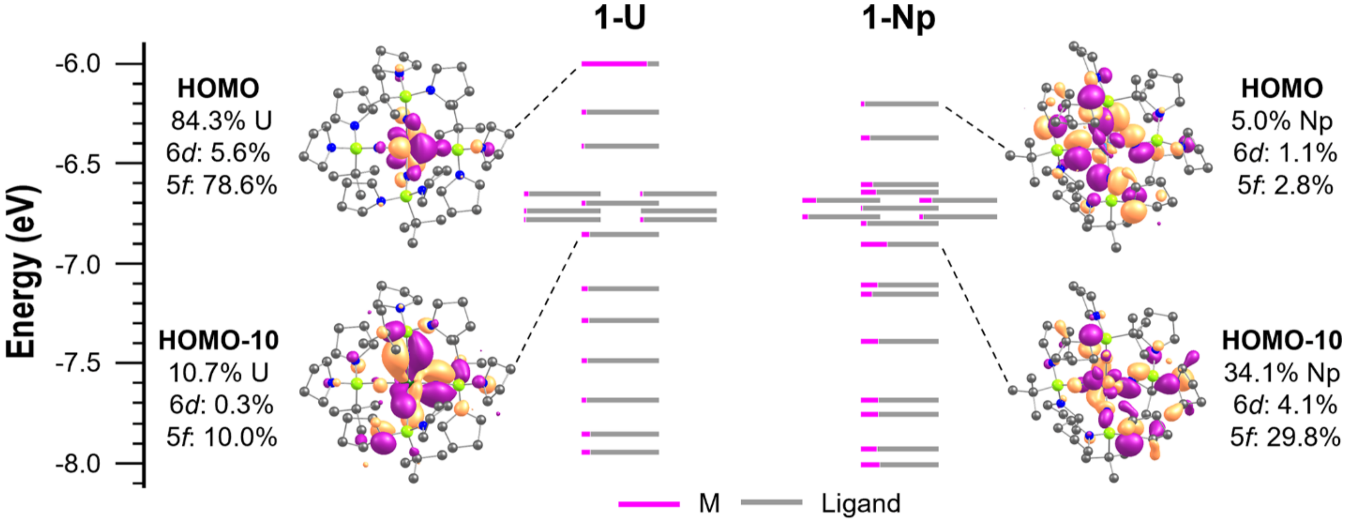

**Figure 3 | Comparative α-MO energy diagrams of 1-U and 1-Np.** Colors of the MO lines represent the percentage of the atomic orbitals of selected fragments in the MOs: metal, magenta; all ligand atoms, gray. Representative MOs specifying metal 6*d*/5*f* characters are displayed on the sides. H atoms are removed for clarity. Degeneracy of the energy levels is set to 0.05 eV for visualization purposes.

The increased metal contribution in the MOs does not necessarily imply a greater M–L covalency. Therefore, Natural Bond Orbital (NBO) [18,19] and Adaptive Natural Density Partitioning (AdNDP)[20] methods were employed to obtain a more chemically intuitive picture of chemical bonding and circumvent extensive delocalization of the canonical MOs. These electron localization methods delineate the metal contributions to the localized non-bonding elements from those describing M–L bonding. As expected for the $Np^{5+}$ and $U^{5+}$ oxidation states, two unpaired electrons were recovered on Np in **1-Np** and one on U in **1-U** with high occupation numbers (ON=0.99-1.00 |e|), displaying dominant 5*f* character (98.4-99.4%) (Fig. S25, S26). M–L interactions are described by four localized two-center two-electron (2c-2e) M–$N_{im}$ σ bonds with ON=1.98 |e| and eight three-center two-electron (3c-2e) M–$N_{im}$–P π bonds with ON=1.94-1.95 |e|, similar to the bonding scheme in the recently reported $U^{6+}$ mono-oxo complex employing the same NPC ligands[14]. While the metal contributions and 6*d*/5*f* characters of the M–N(–P) NBO hybrids are comparable between **1-Np** and **1-U**, the latter exhibits a slightly greater total 6*d*+5*f* orbital population (0.748 |e| *vs*. 0.796 |e|), suggesting somewhat higher orbital overlap (Table S8). To further assess M–L covalency, Quantum Theory of Atoms in Molecules (QTAIM)[21] parameters for bond critical points were evaluated. **1-Np** and **1-U** were found to have similar electron density, ρ, (0.135 $|e|/Bohr^3$ *vs*. 0.136 $|e|/Bohr^3$) for the M–$N_{im}$ interactions, with **1-U** having marginally more negative total energy density, H(r) (-0.056 $Ha/Bohr^3$ *vs*. -0.059 $Ha/Bohr^3$) (Table S9), suggesting slightly more covalent M–$N_{im}$ bonding compared to **1-Np**[22].

The differences in the first coordination sphere caused by the change in the metal oxidation state/identity were further analyzed in correlation with the P–$N_{pyrr}$ bonding (Table S10). Assessing the σ and π bonding contributions from the $N_{pyrr}$ atoms in the P–$N_{pyrr}$ bonds in **1-Np**, NBO analysis shows marginally larger contributions for the $N_{planar}$ atoms compared to $N_{pyram}$ (0.558 |e| *vs*. 0.553 |e|), in agreement with their slightly shorter average bond lengths (1.669 Å for P–$N_{planar}$ *vs*. 1.688 Å for P–$N_{pyram}$). In concordance with previous studies[13,14] the shorter P–$N_{pyrr}$ bonds are indicative of a higher oxidation state of the metal, with both P–$N_{pyram}$/P–$N_{planar}$ bonds exhibiting more covalent interactions in pentavalent **1-Np** than in tetravalent $[Np^{4+}(NPC)_4]$, *i.e.*, 0.553/0.558 |e| *vs*. 0.523/0.530 |e|. Conversely, changing the metal identity results in little to no difference in both $M^{4+}$ and $M^{5+}$ species (Table S10).

## Choice of oxidant

The judicious choice of oxidant is critical in the synthesis of **1-Np**. While oxidation of the analogous uranium complex, $[U^{4+}(NPC)_4]$, to **1-U** is achieved by addition of one equivalent of $[Ag][B(ArF_5)_4]$ [13], $[Np^{4+}(NPC)_4]$ does not react with $[Ag][B(ArF_5)_4]$ under the same conditions. This lack of reactivity is unchanged by the application of heat and/or extension of the reaction time up to 24 hours. Both the limited utility of $[Ag][B(ArF_5)_4]$ as an oxidizing agent and the increasing oxidation potentials across the actinide series are demonstrated here, as the $Np^{5+/4+}$ redox couple is 870 mV more positive than the $U^{5+/4+}$ couple (-1.57 V)[13]. We note that the $Ag^{+/0}$ redox potential can vary widely and is highly dependent on specific reaction conditions[15]. Therefore, AgCl was also explored as a potential inner-sphere oxidant to bracket the accessible potentials for $Ag^+$. The reaction of $[Np^{4+}(NPC)_4]$ with 1 equivalent of AgCl did not proceed in diethyl ether. Replacement of diethyl ether with THF quickly afforded a dark brown product, and after several recrystallizations (see SI for details), a large crystal (~4 x 3 x 2 mm) of **Np-Cl** ($[Np^{5+}(NPC)_2(HNPC)Cl_3]$) was isolated. This result could not be replicated in reactions using 1 or 3 equivalents of AgCl, however, the crystallographic characterization of this second pentavalent, non-neptunyl compound serves as a useful crystallographic and theoretical benchmark for addressing oxidation state ambiguity in heavy element structures.

The location of low-scattering H atoms near actinide centers can be problematic, as electron density deformations that are not accommodated by a spherical atom model are common for actinide complexes. This challenge is well-illustrated by **Np-Cl**. Excellent-quality single crystals of **Np-Cl** were grown, which diffracted well with a resolution of 0.5 Å. There was no apparent disorder or Q-peak indicating the presence of a proton. A converged solution for the complex with a formally hexavalent oxidation state of the neptunium in "$[Np^{6+}(NPC)_3Cl_3]$" was found (Fig. S19, pg. S23). Additionally, no clear justification for the inclusion of a proton could be made based on uniform $N_{im}$=P bond lengths, and large Np–N–P angles for all three ligands. The one notable feature was bond length discrepancy between the mutually *trans* Np–N1/Np-N2 (2.000(7) Å) and the *cis* Np–N3 (2.439(2) Å), for which a strong inverse-trans influence could be implicated[23-29]. While initial attempts to affix the H atom on N3 resulted in an electron density hole (Fig. S19), theoretical investigation of this putative $Np^{6+}$ species through DFT and XMS-CASPT2 calculations indicated that this complex is best formulated as a protonated $Np^{5+}$ complex $[Np^{5+}(\textit{trans}\text{-}NPC)_2(HNPC)Cl_3]$ (Tables S11, S13, Fig. S18). Reinvestigation of the crystallographic model of **Np-Cl** via the electron deformation densities of the Np–N–P bonds showed significantly less density contributed to the *cis*-Np–N bond consistent with protonation of N3 (Fig. S20), and a converged solution was achieved, with nominal changes to bond metrics (Table S11). The proton was freely refined with no positional constraints, as it is highly diffuse and disordered around N3. This analysis demonstrates the critical role of theoretical modeling in verification of transuranic refinement models.

## PCET reactivity of 1-Np

**1-Np** was characterized via NMR spectroscopy in THF-$d_8$, employing a suite of heteronuclear and 2-D experiments. A concentrated sample (~22 mg in 0.3 mL) was prepared and transported to a 400 MHz instrument. In an initial measurement of **1-Np** at t = 2.7 hours[17], three resonances in the $^{31}P\{^1H\}$ spectrum were observed: a primary resonance at 133 ppm corresponding to the $Np^{5+}$ species, and two weaker resonances at 345 ppm and -15 ppm (in a 3:1 ratio, respectively) (Extended Data Fig. 1) belonging to a single product, $[Np^{4+}(NPC)_3(HNPC)][B(ArF_5)_4]$ (**2-Np**, Fig. S15). These latter resonances, which are consistent with two ligand environments on a $Np^{4+}$ species, increase in area in subsequent measurements, while the $Np^{5+}$ resonance area decreases (Extended Data Fig. 1). The changes in $^{31}P\{^1H\}$ peak areas of the two species over ~6.5 hours are consistent with first-order kinetics and an approximate $t_{1/2}$ of 140 minutes for the reaction of **1-Np** in THF-$d_8$ to form **2-Np** (Fig. 4a). **1-Np** and **2-Np** are both uniquely identified in the $^1H$ and $^{13}C\{^1H\}$spectra, and $^{19}F$ NMR displays only one discernable set of resonances (Fig. S4-12).

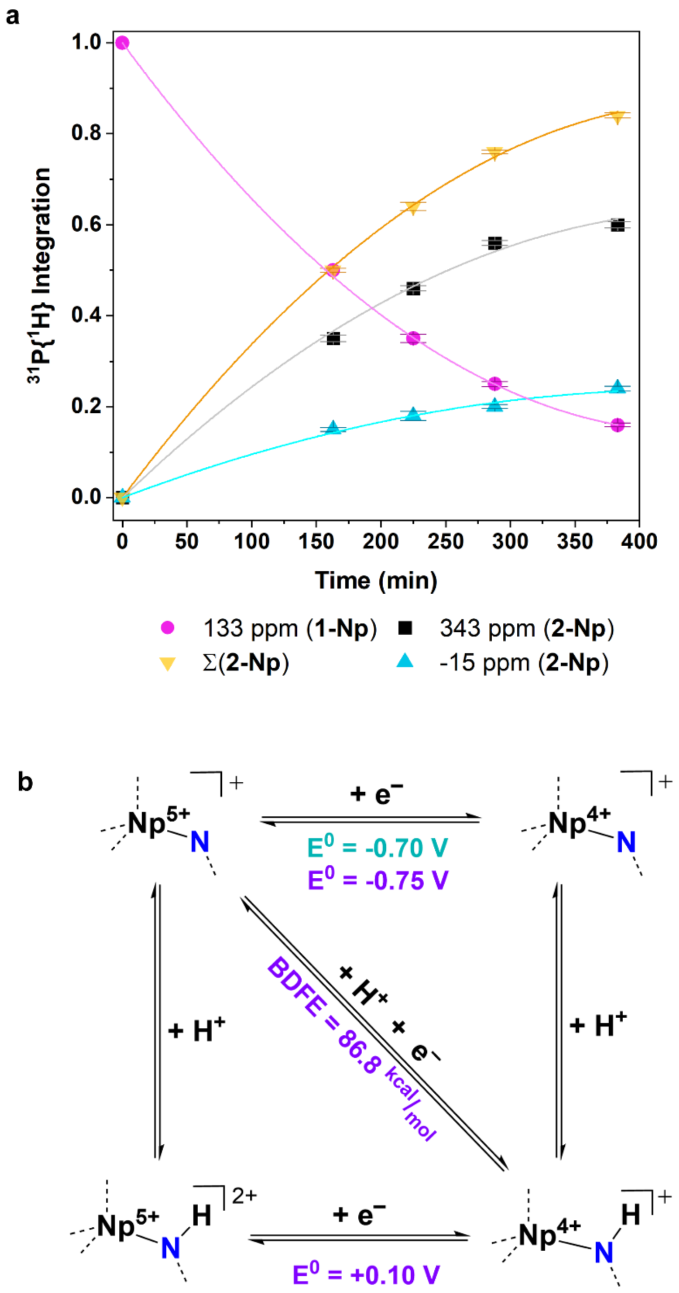

**Figure 4 | PCET reactivity of 1-Np. a,** Plot of $^{31}$P{$^1$H} NMR peak areas (normalized to a sum of 1.0) over 6.4 h showing 1st order decay of **1-Np** into **2-Np** in THF-*d*$_8$ ($t_{1/2}$ = 140 min; $k_{obs}$ = 5 x 10$^{-3}$ min$^{-1}$). Sample prepared at $t_0$ with first measurement at $t_1$ = 2.7 h. Lines are second-order polynomial fits (see SI for details and linear fits). Point 0 input for purposes of fit; **b,** Square scheme for proton coupled electron transfer mechanism with computed (purple) and experimental (teal) values[13].

To further confirm the transformation of **1-Np** to **2-Np** in THF and its solution structural assignment, **2-Np** was independently prepared by stirring 59 mg of isolated **1-Np** in 2 mL of THF at ~20 °C overnight. A gradual color change from opaque brown to orange-pink was observed (Fig. S13). Removal of volatiles and crystallization from a concentrated diethyl ether solution over several days yielded small pale pink crystals, which were identified as the protonated Np$^{4+}$ species **2-Np** ([Np$^{4+}$(NPC)$_3$(HNPC)][B(ArF$_5$)$_4$]) by SC-XRD (Fig. 2B, S15). **2-Np** is tetrahedral ($\tau_4$ = 0.93), featuring three Np–N bonds with an average distance of 2.133(18) Å, consistent with the Np$^{4+}$ oxidation state (Extended Data Table 1). The fourth Np–N bond measures 2.390(7) Å, and features a more drastically compressed Np–N–P angle of 140.2(3)°, unambiguously indicating protonation of the coordinated ligand. This H atom was assigned from the nearby Q-peak and refined well as a proton localized on N1D. The ΣN° values for **2-Np** are bimodal and consistent with the expected range for Np$^{4+}$ species[13], with more rigorously planar pyrrolidinyl N atoms observed. A notable feature of the protonated ligand is the anomalously short P–N$_{pyrr}$ distance of 1.626(6) Å associated with the planar pyrrolidinyl group (ΣN° = 360.0(5)°). The protonated ligand has an elongated P=N$_{im}$ distance (1.582(7) Å) and appreciably higher σ + π contribution from N$_{pyrr}$ than its non-protonated counterparts for both P–N$_{pyram}$ (0.577 |e| *vs*. 0.542 |e|) and P–N$_{planar}$ (0.582 |e| *vs*. 0.549 |e|) bonds, in agreement with their shorter bond distances (Table S10).

Bonding analysis of **2-Np** shows considerable alterations in the Np–N$_{im}$ interactions when compared to tetrahomoleptic [Np$^{4+}$(NPC)$_4$], induced by the protonation of one ligand. The formation of the additional N$_{im}$–H σ bond and disruption of one 3c-2e Np–N$_{im}$–P π bond, causes a reduction of the Np orbital participation in those Np–N$_{im}$ bonds (7.0% σ/3.3% π) (Fig. S29). This results in a compensation of Np orbital participation for the three Np–N$_{im}$ bonds of the non-protonated ligands (10.4% σ/9.7% π), which exhibit greater metal contribution than in [Np$^{4+}$(NPC)$_4$] (10.1% σ/7.2% π), but still less than in pentavalent **1-Np** (14.5% σ/12.1% π). NBO and QTAIM analyses also show that the compensation of the three NPC ligands for the protonated ligand in **2-Np** places them between [Np$^{4+}$(NPC)$_4$] and **1-Np** in terms of Np–N$_{im}$ bond covalency, *e.g.*, 6*d*+5*f* population = 0.572 |e| in **2-Np** *vs*. 0.465 |e| in [$Np^{4+}(NPC)_4$] and 0.748 |e| in **1-Np**, while the protonated ligand exhibits the least covalent Np–$N_{im}$ interaction of all considered complexes, *i.e.*, 6*d*+5*f*=0.195 |e| (Tables S8, S9).

To thermodynamically probe the observed PCET reaction, the bond dissociation free energy (BDFE) of the $N_{im}$–H σ bond in **2-Np** was theoretically evaluated. Based on the experimentally determined free energy of H atom transfer from 1-hydroxy-2,2,6,6-tetramethyl-piperidine (TEMPO-H) in THF[30] (Extended Data Fig. 2), which was previously used to predict the N–H BDFE values for other systems[31], the N–H BDFE of **2-Np** was assessed to be 86.8 kcal/mol. This BDFE is comparable to the experimental value recently reported for a high-valent Fe phosphinimide complex (92 kcal/mol) [32]. Using the computed BDFE for **2-Np** and the experimental $E^0$ (-0.70 V *vs*. Fc/$Fc^+$) in tandem with the Bordwell equation (Eq. S1) indicates that the pKa for the N–H bond of the tetravalent complex is approximately 27.0. Techniques to measure the non-aqueous pKa indirectly (via NMR or electronic absorption spectroscopic titration experiments) with proper radiological containment are in development.

The transformation from **1-Np** to **2-Np** is the first experimentally defined PCET reaction of a transuranic complex in the condensed phase[33,34]. This result opens the opportunity to correlate changes in bonding across the mid-actinides (U-Pu) with changes in the thermochemistry of a fundamental reaction. PCET reactions have been invoked to explain the chemical, electrochemical, and biochemical reduction of hexavalent uranyl and penta- and hexavalent neptunyl, plutonyl, and americyl[35-46], and in the reactions of uranium nitride[47,48] or imido complexes[49]. In these chemical transformations of actinyl moieties, the fundamental PCET reaction step is masked by subsequent reactions including disproportionation, oligomerization, and hydrolysis. The new structural paradigm established here for the stabilization of a high-valent neptunium complex affords the opportunity to quantify the kinetics and thermodynamics of the PCET reaction (an otherwise ubiquitous and critical reaction in bioinorganic and energy conversion processes)[50] in actinide complexes directly.

## References and Notes

1 Dutkiewicz, M. S. *et al.* A terminal neptunium(V)–mono(oxo) complex. *Nat. Chem.* **14**, 342-349 (2022).

2 Brown, J. L. *et al.* A Linear trans-Bis(imido) Neptunium(V) Actinyl Analog: $Np^V(NDipp)_2(^tBu2bipy)_2Cl$ (Dipp = 2,6-$iPr_2C_6H_3$). *J. Am. Chem. Soc.* **137**, 9583-9586 (2015).

3 Eller, P. G., Malm, J. G., Swanson, B. I. & Morss, L. R. Reactions of hexafluorides of uranium, neptunium, and plutonium with nitrogen oxides and oxyfluorides. Synthesis and characterization of (NO)[$NpF_6$] and (NO)[$PuF_6$]. *J. Alloys Comp.* **269**, 50-56 (1998).

4 Dutkiewicz, M. S. *et al.* Organometallic neptunium(III) complexes. *Nat. Chem.* **8**, 797-802 (2016).

5 Asprey, L. B., Keenan, T. K., Penneman, R. A. & Sturgeon, G. D. Alkali fluoride complexes of pentavalent neptunium. *Inorg. Nucl. Chem. Lett.* **2**, 19-21 (1966).

6 Asprey, L. B. & Penneman, R. A. Fluorine Oxidation of Tetravalent Uranium and Neptunium to the Pentavalent State. *J. Am. Chem. Soc.* **89**, 172-172 (1967).

7 Malm, J. G., Williams, C. W., Soderholm, L. & Morss, L. R. Preparation, chemical reactions, and some physical properties of neptunium pentafluoride. *J. Alloys Comp.* **194**, 133-137 (1993).

8 Samulski, E. T. & Karraker, D. G. Some ethoxide compounds of neptunium. *J. Inorg. Nucl. Chem.* **29**, 993-996 (1967).

9 Rice, N. T. *et al.* Homoleptic Imidophosphorane Stabilization of Tetravalent Cerium. *Inorg. Chem.* **58**, 5289-5304 (2019).

10 Rice, N. T. *et al.* Design, Isolation, and Spectroscopic Analysis of a Tetravalent Terbium Complex. *J. Am. Chem. Soc.* **141**, 13222-13233 (2019).

11 Rice, N. T. *et al.* Comparison of tetravalent cerium and terbium ions in a conserved, homoleptic imidophosphorane ligand field. *Chem. Sci.* **11**, 6149-6159 (2020).

12 Rice, N. T. *et al.* Spectroscopic and electrochemical characterization of a $Pr^{4+}$ imidophosphorane complex and the redox chemistry of $Nd^{3+}$ and $Dy^{3+}$ complexes. *Dalton Trans.* **51**, 6696-6706 (2022).

13 Otte, K. S. *et al.* Divergent Stabilities of Tetravalent Cerium, Uranium, and Neptunium Imidophosphorane Complexes. *Angew. Chem. Int. Ed.*, e202306580 (2023).

14 Niklas, J. E., Studvick, C. M., Bacsa, J., Popov, I. A. & La Pierre, H. S. Ligand Control of Oxidation and Crystallographic Disorder in the Isolation of Hexavalent Uranium Mono-Oxo Complexes. *Inorganic Chemistry* **62**, 2304-2316 (2023).

15 Connelly, N. G. & Geiger, W. E. Chemical Redox Agents for Organometallic Chemistry. *Chem. Rev.* **96**, 877-910 (1996).

16 Shannon, R. D. Revised effective ionic radii and systematic studies of interatomic distances in halides and chalcogenides. *Acta Crystallogr. A* **32**, 751-767 (1976).

17 Radiological constraints required for handling (including appropriate containment) and transporting neptunium samples to spectrometers limits the minimum time between dissolution and initial measurement. In the case of electronic absorption spectroscopy ~1 h is necessary. In the case of nuclear magnetic resonance spectroscopy on a sufficiently high field instrument, measurement cannot begin until several hours after sample dissolution.

18 Foster, J. P. & Weinhold, F. Natural hybrid orbitals. *J. Am. Chem. Soc.* **102**, 7211-7218 (1980).

19 Weinhold, F. & Landis, C. R. *Valency and Bonding*. (Cambridge University Press, 2003).

20 Zubarev, D. Y. & Boldyrev, A. I. Developing paradigms of chemical bonding: adaptive natural density partitioning. *Phys. Chem. Chem. Phys.* **10**, 5207-5217 (2008).

21 Bader, R. F. W. Atoms in molecules. *Acc. Chem. Res.* **18**, 9-15 (1985).

22 Cremer, D. & Kraka, E. Chemical Bonds without Bonding Electron Density — Does the Difference Electron-Density Analysis Suffice for a Description of the Chemical Bond? *Angew. Chem. Int. Ed.* **23**, 627-628 (1984).

23 O'Grady, E. & Kaltsoyannis, N. On the inverse trans influence. Density functional studies of $[MOX_5]^{n-}$ (M = Pa, n = 2; M = U, n = 1; M = Np, n = 0; X = F, Cl or Br). *Dalton Trans.*, 1233-1239 (2002).

24 Denning, R. G. Electronic Structure and Bonding in Actinyl Ions and their Analogs. *J. Phys. Chem. A* **111**, 4125-4143 (2007).

25 Minasian, S. G. *et al.* Determining Relative f and d Orbital Contributions to M–Cl Covalency in $MCl_6^{2-}$ (M = Ti, Zr, Hf, U) and $UOCl_5^{-}$ Using Cl K-Edge X-ray Absorption Spectroscopy and Time-Dependent Density Functional Theory. *J. Am. Chem. Soc.* **134**, 5586-5597 (2012).

26 Kosog, B., La Pierre, H. S., Heinemann, F. W., Liddle, S. T. & Meyer, K. Synthesis of Uranium(VI) Terminal Oxo Complexes: Molecular Geometry Driven by the Inverse Trans-Influence. *J. Am. Chem. Soc.* **134**, 5284-5289 (2012).

27 La Pierre, H. S. & Meyer, K. Uranium-Ligand Multiple Bonding in Uranyl Analogues, $[L{=}U{=}L]^{n+}$, and the Inverse Trans Influence. *Inorg. Chem.* **52**, 529-539 (2013).

28 Lewis, A. J., Mullane, K. C., Nakamaru-Ogiso, E., Carroll, P. J. & Schelter, E. J. The Inverse Trans Influence in a Family of Pentavalent Uranium Complexes. *Inorg. Chem.* **53**, 6944-6953 (2014).

29 Köhler, L. *et al.* Insights into the Electronic Structure of a U(IV) Amido and U(V) Imido Complex. *Chem.: Eur. J.* **28**, e202200119 (2022).

30 Wise, C. F., Agarwal, R. G. & Mayer, J. M. Determining Proton-Coupled Standard Potentials and X–H Bond Dissociation Free Energies in Nonaqueous Solvents Using Open-Circuit Potential Measurements. *J. Am. Chem. Soc.* **142**, 10681-10691 (2020).

31 Bruch, Q. J. *et al.* Dinitrogen Reduction to Ammonium at Rhenium Utilizing Light and Proton-Coupled Electron Transfer. *J. Am. Chem. Soc.* **141**, 20198-20208 (2019).
32 Lee, H. B., Britt, R. D. & Rittle, J. N − H bond dissociation free energy of a terminal iron phosphinimine. *J. Coord. Chem.* **75**, 1804-1814 (2022).
33 Warren, J. J., Tronic, T. A. & Mayer, J. M. Thermochemistry of Proton-Coupled Electron Transfer Reagents and its Implications. *Chem. Rev.* **110**, 6961-7001 (2010).
34 Agarwal, R. G. *et al.* Free Energies of Proton-Coupled Electron Transfer Reagents and Their Applications. *Chem. Rev.* **122**, 1-49 (2022).
35 Renshaw, J. C. *et al.* Bioreduction of Uranium: Environmental Implications of a Pentavalent Intermediate. *Environ. Sci. Technol.* **39**, 5657-5660 (2005).
36 Cologgi, D. L., Lampa-Pastirk, S., Speers, A. M., Kelly, S. D. & Reguera, G. Extracellular reduction of uranium via *Geobacter* conductive pili as a protective cellular mechanism. *Proc. Natl. Acad. Sci.* **108**, 15248-15252 (2011).
37 Lovley, D. R., Phillips, E. J. P., Gorby, Y. A. & Landa, E. R. Microbial reduction of uranium. *Nature* **350**, 413-416 (1991).
38 Hou, X., McLachlan, J. R. & Dares, C. J. Electrochemical behaviour of uranium at a tripolyphosphate modified ITO electrode. *Chem. Commun.* **57**, 10891-10894 (2021).
39 Dares, C. J., Lapides, A. M., Mincher, B. J. & Meyer, T. J. Electrochemical oxidation of $^{243}$Am(III) in nitric acid by a terpyridyl-derivatized electrode. *Science* **350**, 652-655 (2015).
40 Hennig, C., Ikeda-Ohno, A., Tsushima, S. & Scheinost, A. C. The Sulfate Coordination of Np(IV), Np(V), and Np(VI) in Aqueous Solution. *Inorg. Chem.* **48**, 5350-5360 (2009).
41 Bender, W. M. & Becker, U. Resolving the kinetics of individual aqueous reaction steps of actinyl ($AnO_2^+$ and $AnO_2^{2+}$; An=U, Np, and Pu) tricarbonate complexes with ferrous iron and hydrogen sulfide from first principles. *Radiochim. Acta* **108**, 165-184 (2020).
42 Faizova, R., Fadaei-Tirani, F., Chauvin, A.-S. & Mazzanti, M. Synthesis and Characterization of Water Stable Uranyl(V) Complexes. *Angew. Chem. Int. Ed.* **60**, 8227-8235 (2021).
43 Faizova, R., Fadaei-Tirani, F., Bernier-Latmani, R. & Mazzanti, M. Ligand-Supported Facile Conversion of Uranyl(VI) into Uranium(IV) in Organic and Aqueous Media. *Angew. Chemie* **132**, 6822-6825 (2020).
44 Bots, P. *et al.* Neptunium(V) and Uranium(VI) Reactions at the Magnetite (111) Surface. *Geosci.* **9**, 81 (2019).
45 Collins, R. N. & Rosso, K. M. Mechanisms and Rates of U(VI) Reduction by Fe(II) in Homogeneous Aqueous Solution and the Role of U(V) Disproportionation. *J. Phys. Chem. A* **121**, 6603-6613 (2017).
46 Wander, M. C. F., Kerisit, S., Rosso, K. M. & Schoonen, M. A. A. Kinetics of Triscarbonato Uranyl Reduction by Aqueous Ferrous Iron: A Theoretical Study. *J. Phys. Chem.* **110**, 9691-9701 (2006).
47 Chatelain, L. *et al.* Terminal uranium(V)-nitride hydrogenations involving direct addition or Frustrated Lewis Pair mechanisms. *Nature Commun.* **11**, 337 (2020).
48 Keener, M., Scopelliti, R. & Mazzanti, M. Nitride protonation and $NH_3$ binding *versus* N–H bond cleavage in uranium nitrides. *Chem. Sci.* **12**, 12610-12618 (2021).
49 Perales, D. *et al.* Conversion of Uranium(III) Anilido Complexes to Uranium(IV) Imido Complexes via Hydrogen Atom Transfer. *Organometallics* **41**, 606-616 (2022).
50 Nocera, D. G. Proton-Coupled Electron Transfer: The Engine of Energy Conversion and Storage. *J. Am. Chem. Soc.* **144**, 1069-1081 (2022).

## Methods

Thorough experimental and theoretical details are available in the Supplementary Information file. A condensed version of the synthesis of **1-Np**, **2-Np**, and **Np-Cl** are included here. All reactions were conducted inside of a negative pressure nitrogen-atmosphere glovebox.

### Synthesis of 1-Np, [Np(V)(NPC)$_4$][B(ArF$_5$)$_4$]

To a 20 ml scintillation vial charged with a stir bar and Np(NPC)$_4$ (0.029 g, 0.024 mmol,) 1 mL of tetrahydrofuran was added. Ferrocenium tetrakis(pentafluorophenyl)borate (0.021 g, 0.025 mmol) was transferred to the reaction vial with 1.5 mL of tetrahydrofuran. On addition, there was an instant color change to dark brown with an orange tint, the color continued to darken over the course of 5 minutes. The reaction mixture was stirred for 30 minutes before the solvent was removed *in vacuo*, affording a brown residue. 1 mL aliquots were used to wash the residue until it was colorless when decanted off, the residue was occasionally scraped with a spatula, and the washes were repeated approximately 10 times. Residual *n*-pentane was removed *in vacuo*, and then the brown residue was redissolved in 1.5 mL of diethyl ether. The filtrate was reduced in volume *in vacuo* and was then placed in a -35 ˚C freezer overnight. Brown XRD quality crystals grew, the solution was decanted, and the remaining volatiles were removed *in vacuo* to afford the title compound (0.038 g, 84%.)

### Synthesis of 2-Np, [Np(IV)(NPC)$_3$(HNPC)][B(ArF$_5$)$_4$]

**1-Np** (0.059 g, 0.031 mmol) was prepared as described above and immediately carried forward. 2 mL of tetrahydrofuran was added with a stir bar to the scintillation vial and the reaction was stirred for 42 hours. The color continued to lighten over the first ~24 hours to a pinkish-orange solution containing a small amount of dark particulate, images of the color change are shown in **S13B**. Volatiles were removed *in vacuo*, affording a foamy solid. The solid was redissolved in 1.5 mL of diethyl ether and filtered through a pipette packed with a glass fiber filter paper and Celite into a 4 mL vial. The filtrate was concentrated *in vacuo* and silicon grease was added to the 20 mL outer vial before moving it to a -35 ˚C freezer. A small quantity of pale pink SCXRD-quality crystals grew over the course of six days.

### Synthesis of Np-Cl, [Np(V)Cl$_3$(NPC)$_2$(HNPC)]

AgCl (0.005 g, 0.033 mmol) was transferred as a suspension into a scintillation vial containing Np(NPC)$_4$ (0.039 g, 0.032 mmol) and a stir bar with three 1 mL aliquots of diethyl ether. No color change was observed after 10 minutes. Volatiles were removed *in vacuo*, and 1-2 mL of tetrahydrofuran were then added. A rapid color change was noted upon solvent change to deep brown with concomitant formation of a grey solid. The volatiles were removed *in vacuo* after 4 hours and the brown residue was triturated with three 0.5 mL aliquots of *n*-pentane. The residue was then taken up in 1 mL of diethyl ether and filtered through a pipette packed with a glass fiber filter paper and Celite. The filtrate was concentrated *in vacuo* to <0.1 mL deep brown solution and stored a -35 ˚C overnight. Some solids formed, but did not appear crystalline, so no separation was performed, and the volatiles were again removed *in vacuo* and the residue was dissolved in *n*-hexane, and filtered through a pipette packed with a glass fiber filter paper and Celite. The filtrate was concentrated *in vacuo* to <0.2 mL *n*-hexane. Orange-brown solids formed over the course of three days. Examination of the solids revealed that they were not crystalline. The residue and solids were then redissolved in diethyl ether and placed in a 4 mL inner vial, and silicon grease was added to the outer 20 mL scintillation vial and stored in the freezer for an additional three days. A single large dark brown-orange crystal formed, which was used to obtain the SC-XRD structure.

**Data Availability:** X-ray data are available free of charge from the Cambridge Crystallographic Data Centre under references CCDC-2280905 (**1-Np**), CCDC-2280906 (**2-Np**), and CCDC-2280907 (**Np-Cl**). Additional spectroscopic, crystallographic, and computational data are included in the supplementary materials. The source datasets generated and/or analyzed during the current study including computational coordinates/energies and processed spectroscopic data have been deposited in the Figshare database under the accession code: [To be included on acceptance].

**Acknowledgments:** We would like to thank Prof. Cory Windorff (NMSU) for his support during laboratory setup and initial transuranic synthesis.

**Funding:** This material is based upon work supported by the U.S. Department of Energy, Office of Science, Office of Basic Energy Sciences, Heavy Element Chemistry program under Award Number DE-SC0019385 (J.E.N., K.S.O., H.S.L.) at the Georgia Institute of Technology. Computational work was conducted at the University of Akron (C.M.S and I.A.P.) and at the University of South Dakota (S.R.C., B.V.) I.A.P. acknowledges computational resources at the Ohio Supercomputer Center and the ARCC HPC cluster at the University of Akron. The studies of S.R.C. and B.V. were supported by the US. Department of Energy, Office of Science, Office of Basic Energy Sciences, Heavy Element Chemistry Program under Award Number DE-SC0023022. S.R.C. and B.V. also acknowledge support of the high-performance computing systems at the University of South Dakota, funded by the National Science Foundation under Award Number OAC-1626516.

**Author contributions:** J.E.N., K.S.O., and H.S.L. conceived the idea presented in this publication. H.S.L., I.A.P., and B.V. supervised the project and acquired funding. J.E.N., K.S.O., and H.S.L. developed the syntheses and performed the spectroscopic characterization. Crystallographic characterization was performed by K.S.O., J.E.N., H.S.L., and J.B. Theoretical calculations and analysis were performed by C.M.S., S.R.C., B.V., and I.A.P. Analysis and visualization were performed by J.E.N., K.S.O., C.M.S., S.R.C., I.A.P., B.V., and H.S.L. The first draft was written by J.E.N., K.S.O., C.M.S., and S.R.C., with contributions from all authors. The manuscript was reviewed and edited by H.S.L., I.A.P., and B.V. with input from all authors.

**Competing interests:** Authors declare that they have no competing interests.

**Additional information:**

Supplementary Information is available for this paper.

Correspondence and requests for materials should be address to Ivan A. Popov, email: ipopov@uakron.edu and Henry S. La Pierre, Email: hsl@gatech.edu.

## Extended Data

### Extended Data Table 1. Selected bond metrics for $An^{5+}$ and $An^{4+}$ species (An = Np, U).

| Bonds | Distance (Å) / Angle (°) | | | | | | | |
|---|---|---|---|---|---|---|---|---|
| | 1-U[a] | | 1-Np | | 2-Np | | Np-Cl | |
| | Exp. | Theor. | Exp. | Theor. | Exp. | Theor. | Exp. | Theor. |
| An–N | 2.101(5) | 2.094 | 2.085(16) | 2.085 | 2.133(18) | 2.119 | 2.000(7) | 1.968 |
| An–N(H) | | | | | 2.390(7) | 2.434 | 2.439(2) | 2.442 |
| P=N | 1.565(12) | 1.581 | 1.569(7) | 1.582 | 1.557(4) | 1.573 | 1.593(6) | 1.595 |
| P=N(H) | | | | | 1.582(7) | 1.613 | 1.595(2) | 1.596 |
| P–$N_{pyrr}$ | 1.662(14) | 1.679 | 1.667(11) | 1.679 | 1.654(11) | 1.679 | 1.647(7) | 1.665 |
| N–An–N/$\tau_4$ | 109(3)/*0.95* | 109.5/*0.99* | 109(2)/*0.96* | 109.5/*0.95* | 109(5)/*0.93* | 109.3/*0.93* | 177.03(6) / 92(2)[b] | 178.3 / 90.8[b] |
| An–N=P | 168(6) | 175.5 | 166(4) | 175.9 | 156(7) | 171.5 | 157(1) | 154.3 |
| An–N(H)=P | | | | | 140.2(3) | 146.1 | 147.5(1) | 143.9 |

[a] Reported in reference 13.

[b] These values correspond to the two unique N–Np–N angles in **Np-Cl**.

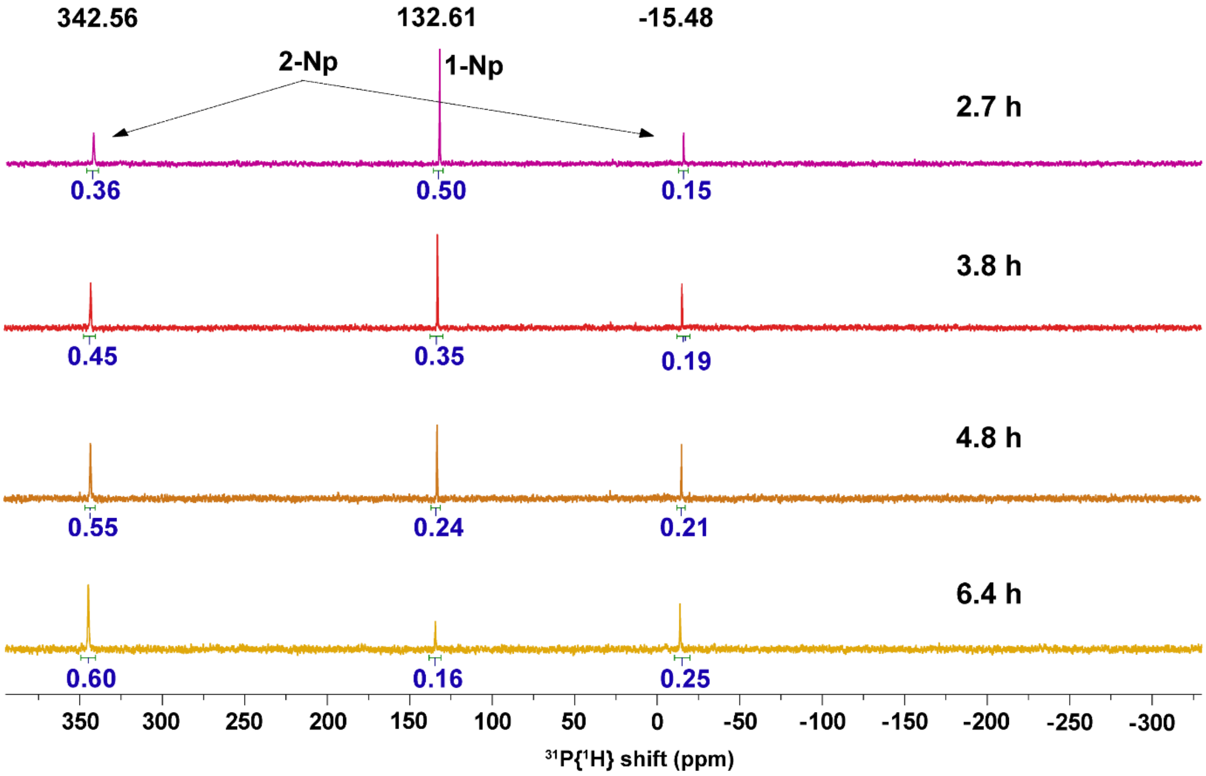

**Extended Data Figure 1 | PCET reactivity on the NMR timescale.** $^{31}P\{^1H\}$ NMR spectra of **1-Np** in THF-$d_8$, prepared at $t_0$ showing loss of **1-Np** and ingrowth of **2-Np** signals. Integration values are normalized to a sum of 1.0 and represent averages over independently processed and integrated data.

$$\begin{array}{ll}
\text{TEMPO} + [\text{Np}^{4+}(\text{NPC})_3(\text{HNPC})]^{+} \rightleftharpoons [\text{Np}^{5+}(\text{NPC})_4] + \text{TEMPOH} & \Delta G_r^{\circ}(\text{H}\bullet) \\
\text{TEMPO} + \text{H}\bullet \rightleftharpoons \text{TEMPOH} & -\Delta_{\text{ref}}\, G_{\text{H}\bullet}^{\circ} \\
\hline
[\text{Np}^{4+}(\text{NPC})_3(\text{HNPC})]^{+} \rightleftharpoons [\text{Np}^{5+}(\text{NPC})_4] + \text{H}\bullet & \Delta G_{\text{H}\bullet}^{\circ}
\end{array}$$

**Extended Data Figure 2 | BDFE calculations.** Thermodynamic equations employed for calculating the N–H bond dissociation free energy of 2-Np through H atom transfer mediated by TEMPO-H.